



Article

Visible Light-Driven Photocatalytic CH₄ Production from an Acetic Acid Solution with Cetyltrimethylammonium Bromide-Assisted ZnIn₂S₄

Monir Uzzaman ^{1,*} , Mst. Farhana Afrin ¹, Mai Furukawa ¹ , Ikki Tateishi ² , Hideyuki Katsumata ¹  and Satoshi Kaneco ^{1,*} 

¹ Department of Applied Chemistry, Graduate School of Engineering, Mie University, Tsu 514-8507, Mie, Japan; farhanaafrin790@gmail.com (M.F.A.); maif@chem.mie-u.ac.jp (M.F.); hidek@chem.mie-u.ac.jp (H.K.)

² Mie Global Environment Center for Education & Research, Mie University, Tsu 514-8507, Mie, Japan; tateishi@gecer.mie-u.ac.jp

* Correspondence: monircu92@gmail.com (M.U.); kaneco@chem.mie-u.ac.jp (S.K.)

Abstract: Photocatalytic methods have been popular in energy production and environmental remediation. Designing high-efficiency photocatalysts is still challenging in converting solar energy into chemical fuels. Herein, a series of surfactant-assisted ZnIn₂S₄ (ZIS) photocatalysts were synthesized by utilizing the one-pot hydrothermal method. Photocatalytic methane production from an acetic acid solution was carried out under LED light (450 nm) irradiation, and the evolved gas was analyzed by the GC-FID system. Reaction factors (surfactant amount, catalyst dose, reaction temperature, substrate concentration, and reaction pH) were optimized for photocatalytic production. With the increase in cetyltrimethylammonium bromide (CTAB) amount, CH₄ production gradually increased. The ZIS-3.75 photocatalyst exhibited the highest photocatalytic CH₄ production rate (0.102 μmol g⁻¹·h⁻¹), which was approximately 1.8 times better than that of pure ZIS (0.058 μmol g⁻¹·h⁻¹). The presence of CTAB reduced the charge transfer resistance and improved photocurrent response efficiency. Structure and morphology were characterized by XRD, FTIR, SEM, TEM, and N₂ adsorption–desorption isotherm analysis. Optical properties were investigated by UV-DRS and PL spectroscopic techniques. The electrochemical evaluation was measured through EIS, Mott–Schottky, and transient photocurrent response analysis. The CTAB-modified catalyst showed excellent stability and reusability, even after five irradiation cycles. Methane production was enhanced by lowering the photogenerated charge transfer resistance and boosting the dispersion of ZIS-3.75 under visible light (450 nm) irradiation.

Keywords: ZnIn₂S₄ photocatalyst; CTAB surfactant; acetic acid; methane; visible light irradiation



Citation: Uzzaman, M.; Afrin, M.F.; Furukawa, M.; Tateishi, I.; Katsumata, H.; Kaneco, S. Visible Light-Driven Photocatalytic CH₄ Production from an Acetic Acid Solution with Cetyltrimethylammonium Bromide-Assisted ZnIn₂S₄. *ChemEngineering* **2024**, *8*, 75. <https://doi.org/10.3390/chemengineering8040075>

Academic Editor: Airio Egidio Rodrigues

Received: 2 April 2024

Revised: 5 July 2024

Accepted: 23 July 2024

Published: 26 July 2024



Copyright: © 2024 by the authors. Licensee MDPI, Basel, Switzerland. This article is an open access article distributed under the terms and conditions of the Creative Commons Attribution (CC BY) license (<https://creativecommons.org/licenses/by/4.0/>).

1. Introduction

With the rapid growth of populations and industries, the demand for high energy has been increasing widely. On the other hand, the depletion of non-renewable energy resources indicates the importance of finding new energy sources. Serious pollution and the emission of greenhouse gases are mainly rising from the combustion of fossil fuels [1]. Hydrocarbons and hydrogen may be replaced with fossil fuels due to their reduced pollution and increased combustion heat values [2]. Some of the human-produced waste from agricultural and food processing plant residues contain high amounts of carbohydrates, which can further be converted to hydrogen and hydrocarbons by utilizing anaerobic fermentation and other chemical treatments [3]. Therefore, organic waste or biomass can be considered as a source for clean, cheap, and eco-friendly production of bio-hydrocarbons [4]. The transformation of organic substances to biogas has become one of the easy and popular methods for energy production [5]. Methane is an essential hydrocarbon with extensive implications for energy, the environment, and industrial operations. Compared to coal and oil-based fuels, methane

burns cleaner and releases less CO₂. It can be used as fuel (in heating, cooking, electricity generation, and automobile), the starting material of hydrogen production, and in common valuable chemical synthesis [6].

The photocatalytic methods can be generally used in energy conversion and bacterial disinfection due to their relatively stable and cheaper system [7]. Also, they are successfully applied to the treatment of industrial, pharmaceutical, textile, and tenure waste [8]. Moreover, semiconductor-based photocatalysts such as doping or modified catalysts, nanostructured catalysts with bigger surface areas, and catalyst composites with co-catalysts and sacrificial agents have been utilized in methane production from organic sources, water splitting to produce hydrogen and oxygen, CO₂ reduction to generate hydrocarbon fuels, the removal of pollutants, nitrogen fixation, hazardous treatment, and the synthesis of organic compounds [1]. The photocatalytic process includes light absorption to produce electron-hole pairs, separation of charge, migration of holes and electrons to the photocatalytic surface, electron-hole pair recombination, and the redox reaction on the surface by utilizing produced charges [9,10]. The delayed electron-hole pair recombination favors the photocatalytic reactions [11]. Although semiconductor-based photocatalysts are widely used as clean and environmentally friendly agents, they still have some limitations on photogenerated charge separation and light absorption [8]. Several methods, such as metal and nonmetal doping, vacancy engineering, surface modification, and composite formation, have recently been selected to achieve high photocatalytic activity [12].

So far, many researchers have developed numerous types of photocatalysts, such as metal oxide (TiO₂, ZnO, SnO₂, Fe₂O₃, WO₃, and CeO₂) [13], metal chalcogenides [14], and metal-free graphitic carbon nitride (g-C₃N₄) [15]. Among them, ZnIn₂S₄ (ZIS) is an excellent photocatalyst with a layer structure, good chemical stability, and non-toxic properties and has cubic, trigonal, and hexagonal structures [16,17]. The photocatalytic efficiency of pure ZIS is relatively lower due to the rapid electron-hole pair recombination, lower range of visible light absorption and photocurrent response, and higher charge transfer resistance [18]. The photocatalytic properties of photocatalysts are influenced by morphology, size, band gap, and dimensionality [19]. Structural and morphological controlling can be the alternative way to improve the photocatalyst for higher production [20]. Using surfactants to fabricate the photocatalyst has become one of the most effective ways to mediate the nanostructures to change their crystal structure, surface morphology, and light-harvesting capability, boosting charge separation and migration efficiency. In 2008, Shen et al. reported the improved photocatalytic efficiency of ZIS due to the assistance of surfactants (CTAB, cetylpyridinium bromide, sodium dodecyl sulfate) [21,22]. Metal- (Cu, Ni, Co, Ru, Mo, and Fe) and nonmetal (O, N, and P)-doped ZIS and composite forms of ZIS were successfully applied to hydrogen production [10].

In the 1970s, Kraeutler and Bard first reported the photocatalytic hydrocarbon production from organic compounds. In the study, a Pt/TiO₂ photocatalyst under UV irradiation was used for the decarboxylation of CH₃COOH and CH₄ and CO₂ evolved as the main products from the system by the photo-Kolbe reaction [23]. Further, Mozia et al. investigated the Fe/TiO₂ catalytic degradation of CH₃COOH for the hydrocarbons and hydrogen production under UV light (365 nm) at 25 °C [24]. Heciak et al. [25] and Amorós-Pérez et al. [26] studied the catalytic production of biogas and hydrogen with Cu/TiO₂ under UV light at room temperature.

However, there is little information on photocatalytic CH₄ production under visible light irradiation. Therefore, the present work has mainly dealt with the CATB-assisted ZIS photocatalytic methane production from acidic acid under LED light (450 nm) irradiation. This method can work under atmospheric conditions and without noble metal. Instead of expensive noble metal (Pt), earth-abundant and cheap elements (Zn, In, S) were used as cost-effective photocatalysts for industrial requirements. The surfactant-assisted photocatalyst was relatively stable for several cycles.

2. Experimental

2.1. Materials

All the reagents were analytical grade and used as received without further purification. $\text{ZnSO}_4 \cdot 7\text{H}_2\text{O}$ (99.5%), $\text{InCl}_3 \cdot 4\text{H}_2\text{O}$ (99.9%), CTAB (99.0%), and thioacetamide (99.9%) were purchased from FUJIFILM Wako Pure Chemical Corporation and CH_3COOH (99.8%) was purchased from Sigma-Aldrich (Tokyo, Japan).

2.2. Synthesis of ZnIn_2S_4 (ZIS)

The ZIS nanosheet was synthesized by the hydrothermal route with a minor modification [27]. In detail, 1.0 mmol of $\text{ZnSO}_4 \cdot 7\text{H}_2\text{O}$, 2.0 mmol of $\text{InCl}_3 \cdot 4\text{H}_2\text{O}$, and 8 mmol of thioacetamide were dissolved in 40 mL of deionized water and vigorously stirred at room temperature for 10 min. Next, the mixed suspension was transferred into a 100 mL Teflon-lined stainless still autoclave and heated to 160 °C for 1.0 h. It was reported that the photocatalytic performance of ZIS decreased by prolonging the hydrothermal time; in contrast, catalytic efficiency increased with the increase in CTAB [21]. After cooling to room temperature, the sample was collected by centrifugation, washed several times using ethanol and deionized water, and dried at 60 °C for 12 h. The obtained product (ZnIn_2S_4) was denoted ZIS-0. For the surfactant-assisted photocatalyst synthesis, the same procedure was performed, adding 0.75, 1.75, 2.75, and 3.75 mmol of CTAB into the reaction mixture. The product was named ZIS-x ($x = 0.75, 1.75, 2.75, \text{ and } 3.75$ mmol of CTAB, respectively).

2.3. Characterization

The crystal structure of the prepared samples was investigated using X-ray diffraction (XRD, Rigaku RINT Ultima-IV diffractometer by $\text{Cu K}\alpha$ radiation in a scan range of 10–80 °C at a scan rate of 0.04°/s) and Fourier-Transform Infrared (Perkin Elmer spectrometer (Waltham, MA, USA), SPECTRUM 100 FT-IR) with an attenuated total reflection assemblage. The surface morphology was surveyed by scanning electron microscope (JEOL JEM-1400 Flash SEM, JEOL LTD., Tokyo, Japan) and transmission electron microscope (JEOL JEM-1011 TEM) analysis. Brunauer–Emmett–Teller (BET) surface area was calculated utilizing BELPREP-Vac II (BEL, Tokyo, Japan). Optical properties were investigated by UV-vis diffuse reflectance sorption (DRS) spectroscopy (JASCO V-750 UV-vis instrument equipped by an integrating sphere adaptor) and photoluminescence (PL, Shimadzu fluorescence spectrophotometer (Kyoto, Japan), RF-5300PC) spectroscopic measurement. The electrochemical properties such as electrochemical impedance spectroscopy (EIS), Mott–Schottky plot, and transient photocurrent response (TPCR) measurements were carried out on an electrochemical Versa STAT 3 workstation (Princeton Applied Research) equipped with a conventional three-electrode system. Here, the uniform slurry of the sample by the Nafion solution was coated on a fluorine-doped tin oxide glass plate to make the working electrode, and an aqueous solution of Na_2SO_4 (0.5 mol L^{-1}) was utilized as the electrolyte. Pt wire and AgCl/Ag saturated KCl were used as counter electrodes and reference electrodes, respectively.

2.4. Photocatalytic Methane Production

The photocatalytic CH_4 evolution experiments were performed in a heat resistance Pyrex glass vessel (inner volume: 123 mL); the photocatalyst (75 mg) was dispersed in 40 mL of CH_3COOH (1.0 mol/L) solution, and then the reaction mixture was heated to 50 °C with constant stirring and illuminated by visible LED light (450 nm) for 5 h. Finally, the produced methane was determined every 2.5 h by gas chromatography (GC-353B, GL Science, Tokyo, Japan) using a flame ionization detector (FID). The column was packed with Porapak Q (mesh, 80–100), and the carrier gas was N_2 (99.9%, 29.5 mL/min). The apparent quantum yield (AQY) for the methane production was measured at a 450 nm wavelength using the following equation:

$$\text{AQY} = (\text{nN}_e/\text{N}_p) \times 100 \quad (1)$$

where n , N_e , and N_p denote the electron number required for one methane molecule production, the number of methane molecules, and the number of incident photons, respectively.

3. Results and Discussion

3.1. X-ray Diffraction (XRD) Analysis

The phase and crystal structure of the synthesized photocatalysts were characterized by powder XRD analysis (Figure 1a). Diffraction peaks with 2θ values of 21.64° , 27.74° , 47.6° , 52.4° , 55.48° , and 76.24° can be attributed to the (006), (102), (112), (1012), (202), and (213) planes, respectively. The XRD patterns of both samples present almost similar profiles, and the observed diffraction peaks can be indexed as the pure hexagonal phase of ZIS [22]. No other contaminants were identified, including ZnS, In_2S_3 , oxides, or organic compounds associated with the reactants. Since another two peaks were observed at (104) and (108) for ZIS prepared without CTAB, the difference in their microstructures could be observed. Further, the position of the (006) diffraction peak would be shifted to a lower angle in the presence of CTAB. This means that CTAB was inserted into the layered crystal structure of ZIS. The interlayer distance was enlarged from 4.10 \AA to 4.25 \AA along the c -axis during the hydrothermal operation [21,22].

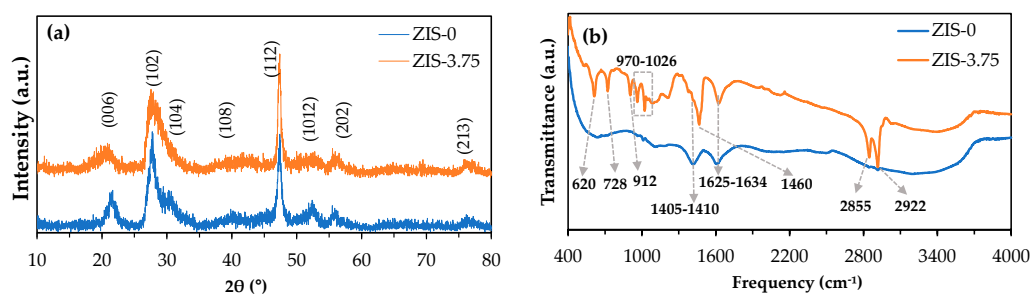


Figure 1. (a) XRD patterns and (b) FTIR spectra of ZIS-0 and ZIS-3.75.

3.2. Fourier-Transform Infrared (FTIR) Spectroscopic Analysis

FTIR spectral data of pure and CTAB-modified ZIS were collected in the $400\text{--}4000 \text{ cm}^{-1}$ range to investigate the chemical structure and the presence of expected functional groups (Figure 1b). The broad absorption peaks around $1625\text{--}1634 \text{ cm}^{-1}$ [28] and $1405\text{--}1410 \text{ cm}^{-1}$ [29] are attributed to the adsorbed water molecules and surface hydroxyl vibration of ZIS-0 and ZIS-3.75. In ZIS-3.75, the C–H symmetric and asymmetric stretching vibrational peaks were observed at 2855 and 2922 cm^{-1} , attributed to the alkyl chain originating from the presence of the CTAB molecule over ZIS, respectively. The peaks at 728 , 970 , and 1460 cm^{-1} could be assigned to the Br^- of CTAB, the out-of-plane C–H vibration of CH_3 , and the symmetric stretching vibration of $\text{N}^+\text{--CH}_3$, respectively [30–32]. The vibrational frequency at 912 and 1025 cm^{-1} is attributed to C–N and C–O stretching, respectively [33–35]. The band at 620 cm^{-1} suggests an interaction between the ZIS surface and chemisorbed CTAB molecules [32]. However, the vibrational signals of the S–In–S–In–S–Zn–S bonds in ZnIn_2S_4 cannot be detected due to their inorganic semiconductor features [36,37].

3.3. Scanning Electron Microscopic (SEM) and Transmission Electron Microscopic (TEM) Analyses

To investigate microstructure and surface morphology, SEM and TEM characterizations were carried out. As shown in Figure 2a,b, ZIS-0 has a large number of honeycomb-like microstructures formed by stacking lamellar structural units on the surface of a single sphere. For ZIS-3.75, the arrangement of lamellar structural units becomes slightly orderly due to the structural guidance of CTAB and the microspherical lamellar gave flower-like structures, indicating that the loading of CTAB has changed the shape and surface of ZIS [22,38]. Elemental mapping using energy-dispersive X-ray spectroscopy (EDS) was carried out to investigate the distribution of the major constituents of the catalysts. The EDS mapping confirms the uniform Zn, In, and S distribution throughout the catalyst

(Figure 2e,f). In the TEM image, the microsphere shape of a pristine ZIS-0 was composed of disordered sheetlike aggregates, while ZIS-3.75 grown into monodisperse micro-flowers was composed of ZnIn_2S_4 petals/sheets in a more regular manner (Figure 2d) [39].

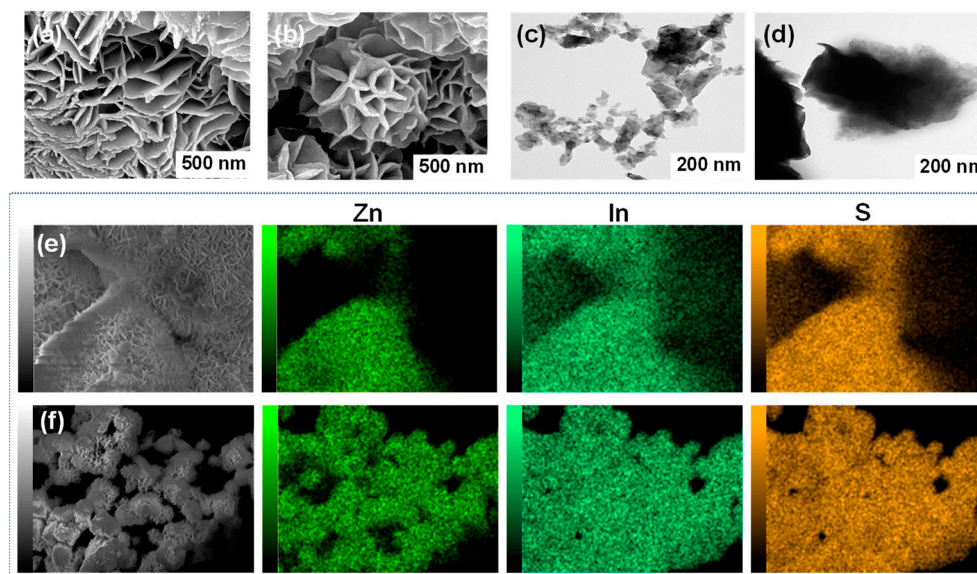


Figure 2. (a,b) SEM and (c,d) TEM images and (e,f) elemental mapping of ZIS-0 and ZIS-3.75, respectively.

3.4. Brunauer–Emmett–Teller (BET) Surface Area and Pore Size Analysis

The specific surface area and pore diameter for ZIS-0 and ZIS-3.75 were investigated by N_2 adsorption–desorption isotherm analysis at 77 K (Figure 3, Table 1). As shown in Figure 3a, ZIS-0 and ZIS-3.75 exhibited IV-type adsorption–desorption, with H2 and H3-type hysteresis loops appearing between P/P_0 values of 0.4 and 1.0, suggesting their mesoporous structure [40–42]. Meanwhile, the surface area values of ZIS-0 and ZIS-3.75 are 18.80 and 6.63 m^2/g , respectively. The assistance of CTAB decreased the surface area and pore volume and increased the pore diameter. Although it can be considered that a larger surface area may generally increase methane production, the surface area had little contribution to acetic acid degradation.

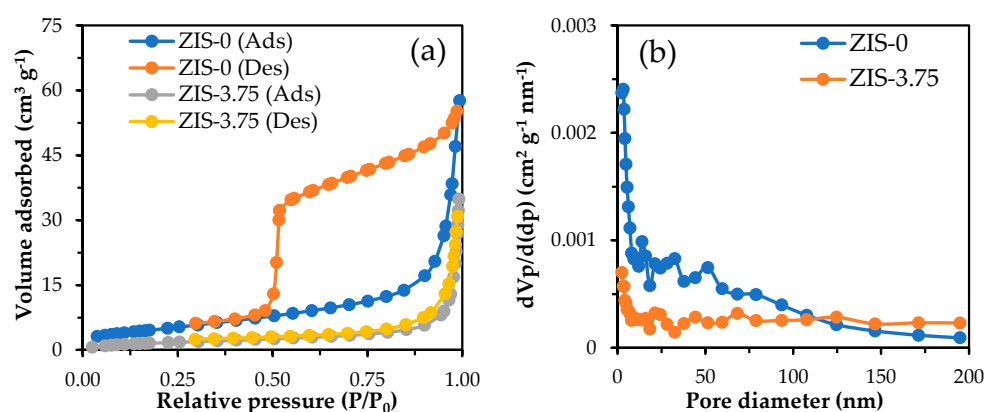


Figure 3. (a) N_2 adsorption–desorption isotherm and (b) corresponding pore size distribution of ZIS-0 and ZIS-3.75.

Table 1. BET surface area (S_{BET}), pore volume (V_{pore}), and pore diameter (D_{pore}) of ZIS-0 and ZIS-3.75.

Photocatalyst	S_{BET} (m^2/g)	V_{pore} (cm^3/g)	D_{pore} (nm)
ZIS-0	18.80	0.085	18.08
ZIS-3.75	6.63	0.052	31.35

3.5. Ultraviolet–Visible Diffuse Reflectance Spectroscopic (DRS) Analysis

The light-absorption capability and energy band structures of ZIS-0 and ZIS-3.75 were calculated using UV-vis DRS measurement and Tauc plot analysis, respectively. The absorption edge of both samples was between 510 and 540 nm in the visible light range (Figure 4a). The absorption edge of ZIS-0 was obtained at 540 nm; on the contrary, a blue shift (510 nm) was observed for the CTAB-assisted ZIS-3.75 catalysts. The steep shape of the visible edge and absorption in the visible light area reveal that the absorption band of ZIS is ascribed to the transition from the valance band to the conduction band [43]. The energy bandgap of the catalysts was calculated using the Taucplot equation as follows:

$$\alpha h\nu = A(h\nu - E_g)^n \quad (2)$$

where α denotes the absorption coefficient, n is 1/2 for the direct bandgap, h is the Planck constant, ν is the light frequency, A is the characteristic constant, and E_g is the bandgap energy. The energy band gap of ZIS-0 was 2.61 eV, and ZIS-3.75 had a greater band gap of 2.77 eV (Figure 4b). The energy band gap was increased in the case of CTAB assistance due to the small crystallite size and different particle morphology. In semiconductor-based photocatalytic reactions, photogenerated electrons (e^-) and holes (h^+) migrate to the surface and act as redox sources. It is widely acknowledged that a stronger redox capacity is correlated with a greater band gap energy because it improves the thermodynamic driving force for water reduction [21]. Methane production may be preferable for the valance band in a relatively positive position.

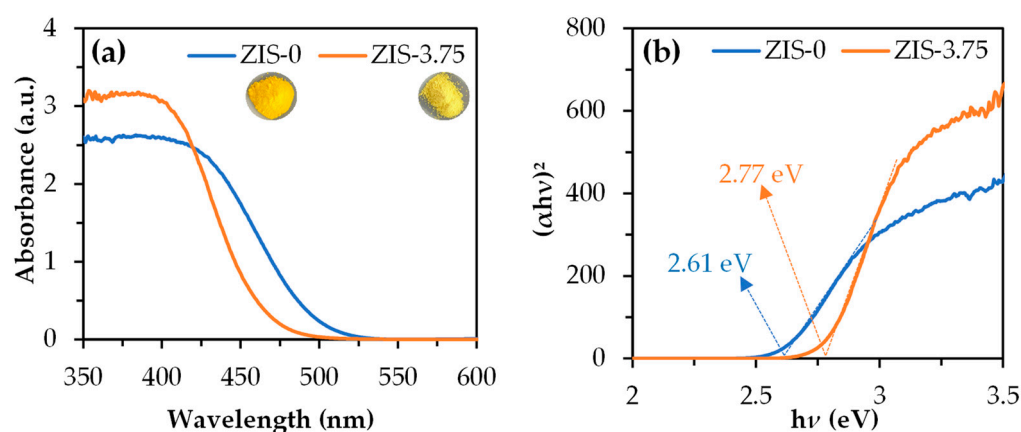


Figure 4. (a) DRS spectra and (b) a Tauc plot for ZIS-0 and ZIS-3.75 photocatalysts.

3.6. Mott–Schottky Analysis

The flat band potential (E_{fb}) and conduction band potential (E_{CB}) positions were measured by Mott–Schottky curve analysis, as depicted in Figure 5a,b. The flat band potentials of ZIS-0 and ZIS-3.75 are -0.71 V and -0.69 V (vs. Ag/AgCl, sat. KCl at pH 7), respectively. The values were converted to -0.10 V and -0.08 V (vs. normal hydrogen scale electrode (NHE) at pH = 0) by utilizing the following equation [44]:

$$E(\text{NHE at pH} = 0) = E(\text{Ag/AgCl at pH} = 7) + 0.196 + 0.059 \times 7 \quad (3)$$

Based on the previous report, the n-type semiconductor materials have a CB potential of approximately 0.1 eV lower than the E_{fb} [45]. Therefore, the conduction band of ZIS-0 and ZIS-3.75 is -0.20 and -0.18 V (vs. NHE at pH = 0), respectively. Further, the valance band position was calculated using the following formula:

$$E_g = E_{VB} - E_{CB} \quad (4)$$

Since the energy band gap of ZIS-0 (2.61 eV) and ZIS-3.75 (2.77 eV) were determined from the Tauc plot (Figure 4b), their valance bands were 2.41 and 2.59 V (vs. NHE at pH = 0), respectively.

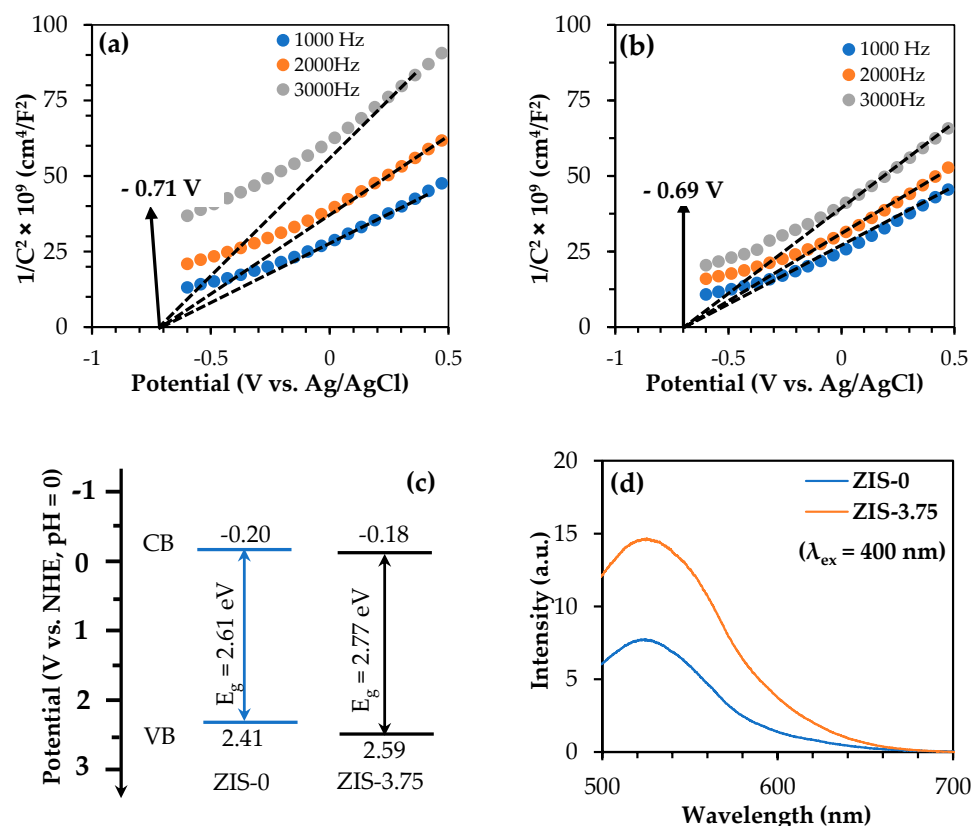


Figure 5. Mott-Schottky plot: (a) ZIS-0 and (b) ZIS-3.75. (c) Band structure and (d) PL spectra.

3.7. Photoluminescence (PL) Analysis

The separation and migration efficiency of photoinduced electron–hole pairs in the photocatalysts were elucidated by PL spectral analysis at the exciting wavelength of 400 nm (Figure 5d). The lower fluorescence intensity represents the reduced recombination of the photogenerated electron–hole pair. The emission intensity of ZIS-0 was lower than that of ZIS-3.75, which suggests that ZIS-0 may hinder the hole pair recombination compared to ZIS-3.75. In the present work, the photocatalytic efficiency of ZIS-3.75 was relatively better than that of ZIS-0. This means that other factors, such as charge transfer resistance and transient photocurrent response, were responsible for improving the photocatalytic efficiency of ZIS-3.75 [46].

3.8. Electrochemical Impedance Spectroscopy (EIS) and Transient Photocurrent Response (TPCR) Analysis

The charge transfer resistance of the interface between the catalyst surface and solvent was measured by EIS analysis [47]. Generally, the charge transfer resistance decreases with the decrease in curvature radius size. Since the Nyquist plot (Figure 6a) ZIS-3.75 has a smaller radius than that of ZIS-0, the result showed the rapid photogenerated carrier separation and charge transfer efficiency of ZIS-3.75. Figure 6b illustrates the TPCR for ZIS-0 and ZIS-3.75 in five cycles. Because the pure ZIS has a relatively lower photocurrent response than that with ZIS-3.75, the CTAB surface assistance improved electron–hole pair separation efficiency.

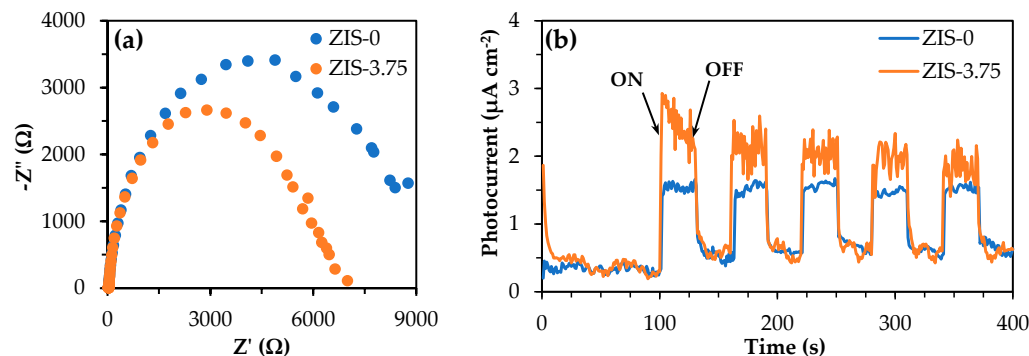


Figure 6. (a) EIS Nyquist plot and (b) TPCR of ZIS-0 and ZIS-3.75.

3.9. Photocatalytic Methane Production

The CTAB-assisted ZIS was applied to the methane production under visible light irradiation (450 nm) in order to assess the photocatalyst performance (Figure 7). First, the photolysis, catalytic reaction, and photocatalytic background reaction without acetic acid were evaluated for comparison with photocatalytic CH_4 production from an acetic acid solution. For the photolysis and catalytic reaction, a trace amount of methane was generated during the irradiation time of 24 h. In the photocatalytic background reaction without acetic acid, 0.25, 0.73, and 0.99 $\mu mol\ g^{-1}$ methane productions were observed for ZIS-0, ZIS-1.75, and ZIS-3.75, respectively. On the other hand, the photocatalytic CH_4 production from the acetic acid solution was obtained with 1.26, 3.27, and 3.89 $\mu mol\ g^{-1}$ amounts, respectively. Consequently, the net productions (0.76, 2.28, and 2.64 $\mu mol\ g^{-1}$) could be realized for the photocatalytic CH_4 production from the acetic acid solution with ZIS, respectively.

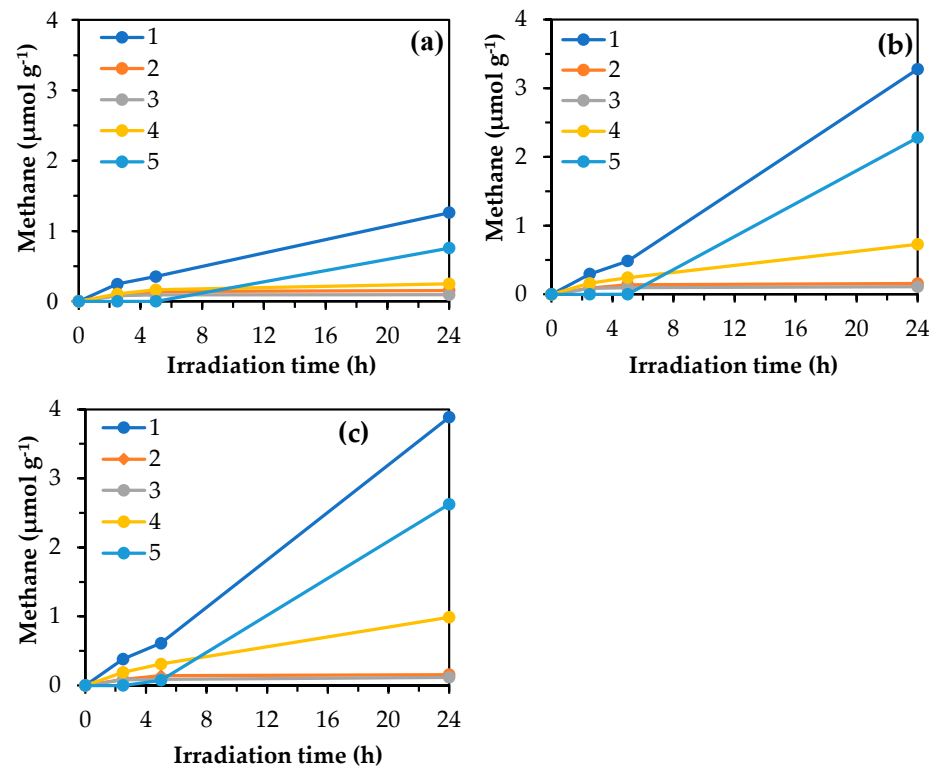


Figure 7. 1—Photocatalytic CH_4 production from the acetic acid solution with ZIS, 2—photolysis from the acetic acid solution under irradiation, 3—catalytic reaction from the acetic acid solution with ZIS under dark conditions, 4—photocatalytic background reaction on ZIS without acetic acid under irradiation, 5—net production of $CH_4 = 1 - (2 + 3 + 4)$. (a) ZIS-0, (b) ZIS-1.75, and (c) ZIS-3.75.

Figure 8a discloses that methane production increased with the increase in irradiation time and CTAB incorporation. As shown in Figure 8b, ZIS-0 evolved a relatively smaller amount of methane, although the production increased gradually with the increase in CTAB incorporation. The maximum production was achieved with ZIS-3.75. The AQY values of ZIS-3.75 were obtained at 450 nm using methane production and incident photons, and they reached 0.006%.

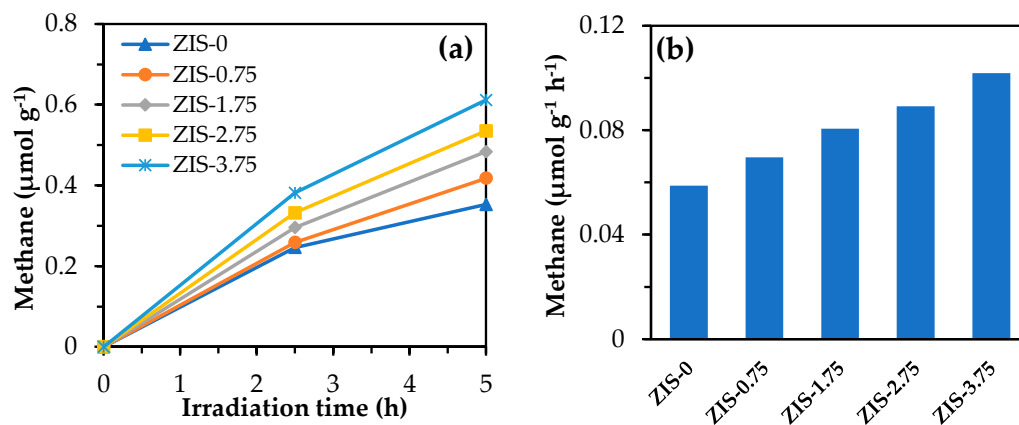


Figure 8. (a) Effect of CTAB amount on photocatalytic methane evolution under visible light irradiation (5 h) and (b) comparison of methane production rates.

3.10. Photocatalytic Performance Conditions

Several operational parameters, such as catalyst loading, reaction temperature, substrate concentration, and solution pH, can influence the redox reaction and photocatalytic efficiency. Therefore, the reaction factors have been investigated for the optimum conditions.

3.10.1. Effect of Catalyst Loading

Since the amount of catalyst loading can significantly affect CH_4 production, it is important to test the optimum loading for effective production in order to avoid the overuse of catalysts. In Figure 9a, with the increase in catalyst loading from 0 to 75 mg, the photocatalytic efficiencies increased sharply and a further increase in catalyst loading remarkably reduced the methane production. During the lower photocatalyst concentration, the reaction is mainly controlled by active sites, which are available for the adsorption of reactants. With the increase in photocatalyst loading, the number of photon absorptions also increased, and the photocatalytic efficiencies improved. The excess catalyst loading may be responsible for the coagulation of particles and light blockage on the catalyst surface, resulting in a decrease in catalytic activity for methane evolution [48].

3.10.2. Effect of Reaction Temperature

Though most photocatalytic reactions were carried out at room temperature, the increase in temperature can significantly influence the photocatalytic reaction rate [49]. By increasing the reaction temperature from 25 to 50 °C, the photocatalytic methane production sharply increased due to the improvement of the charge carrier mobility and interfacial charge transfer capability (Figure 9b). In the temperature range of 50 to 70 °C, the production remained almost constant due to the increased electron–hole pair recombination rate at relatively high temperatures [50].

3.10.3. Effect of CH_3COOH Concentration

The effect of the initial concentration of the substrate on photocatalytic CH_4 production was studied (Figure 9c). It was observed that methane production gradually increased with the increase in the initial concentration from 0 to 1.0 mol/L. Then, with increasing the value, the methane evolution sharply decreased. Due to the increment of substrate concentration,

more organic substances are adsorbed on the catalyst surface, and the reactants have less mobility in the catalyst surface [51].

3.10.4. Effect of pH

The adsorption and dissociation of the reactant are significantly influenced by charge on the photocatalyst surface and pH in the photocatalytic process. To assess the pH effect on photocatalytic CH_4 production, the reaction was conducted by varying the pH from 1.5 to 3.5. The point zero charge (pzc) for ZIS was approximately $\text{pH} = 3.91$ [52] when the charge on the photocatalyst surface was zero, resulting in there being no interaction with the acetic acid [53]. The pzc of ZIS and dissociation constant (pK_a) of acetic acid ($\text{pK}_a = 4.76$) also influence the degradation in a photocatalytic process. The surface of the ZIS photocatalyst is positively charged when the pH is less than pH_{pzc} , and the surface is negatively charged when the pH is more than pH_{pzc} . At a low pH value ($\text{pH} < \text{pK}_a$), acetic acid remains unchanged, whereas the acetate ions (CH_3COO^-) are generated at a high pH value ($\text{pH} > \text{pK}_a$). At $\text{pH} > \text{pH}_{\text{pzc}}$, the surface of the ZIS photocatalyst is negatively charged and the adsorption of CH_3COO^- ions on the ZIS surface is difficult due to static repulsion [54–56]. In this study, CH_4 production primarily increased when the initial pH increased from 1.5 to 3.0 (Figure 9d), and further increases in pH to 3.5 reduced CH_4 production. Several studies have demonstrated the contribution of pH and charge on the photocatalyst surface to the degradation of various mono- and dicarboxylic acids, including formic acid [54,57], acetic acid, propanoic acid, butanoic acid [58,59], oxalic acid, maleic acid, and fumaric acid [60].

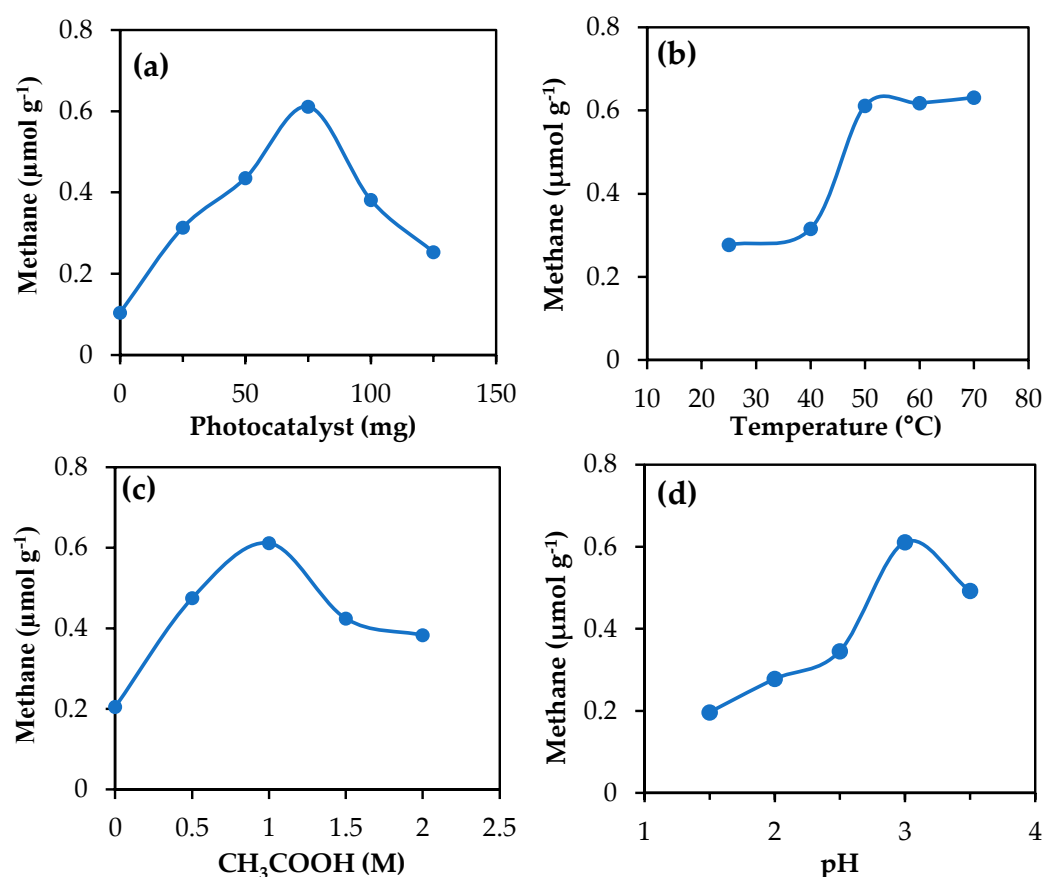


Figure 9. Effects of (a) catalyst amount, (b) reaction temperature, (c) substrate concentration, and (d) pH on photocatalytic methane production with ZIS-3.75.

4. Stability and Reusability Test

Longevity and reusability are crucial factors for the realistic commercial application of photocatalysts. Stability and reusability were assessed by conducting cyclic methane production for up to five consecutive cycles. ZIS-3.75 was used as a photocatalyst under optimum conditions, and the reactor was fully evacuated before starting a new cycle. The methane production slightly increased in the second cycle and remained almost the same as the first cycle up to the fourth cycle, and a slight decrease was observed in the fifth cycle. The results indicated excellent stability, durability, and reusability (Figure 10a). Further, after the reaction, ZIS-3.75 was subjected to SEM, TEM, XRD, and FTIR analysis to reassess and compare its structural and morphological properties. Little significant change could be observed before and after the photocatalytic reaction (Figure 10b–g).

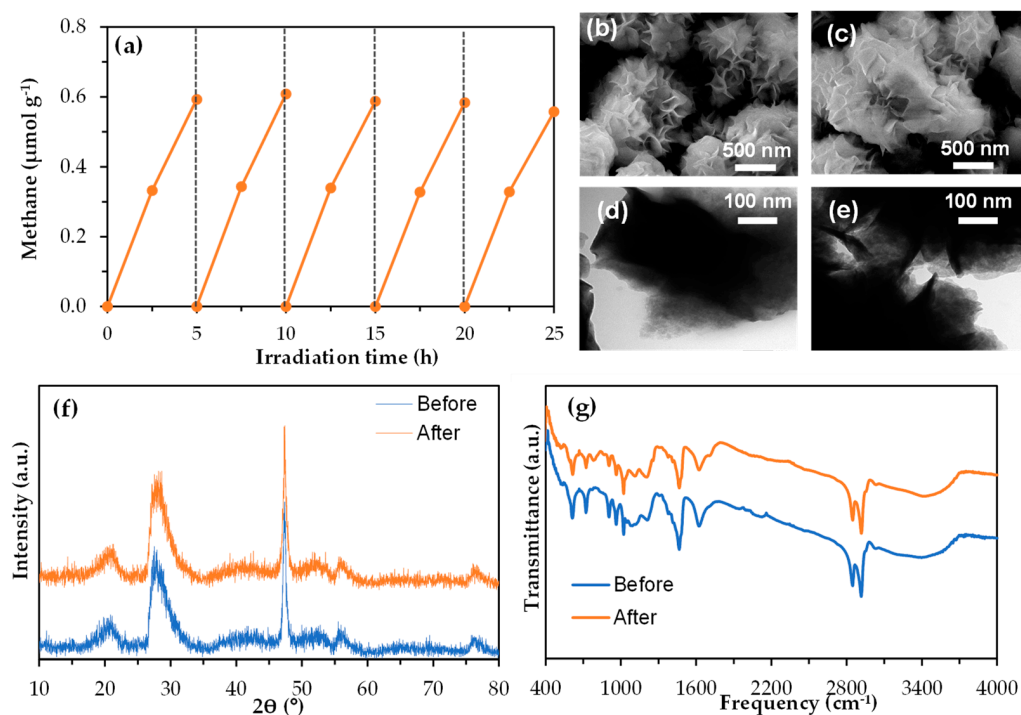


Figure 10. (a) Stability test results, (b,c) SEM images, (d,e) TEM images, (f) XRD patterns, and (g) FTIR spectra of ZIS-3.75 before and after irradiation, respectively.

5. Proposed Mechanism

Based on the above results, a probable degradation of acetic acid and the methane gas production mechanism has been proposed in Figure 11. The whole reaction process can be divided into two stages. In the initial stage, there exists a water-splitting process on the ZIS surface. When light energy larger than the ZIS bandgap is absorbed by the ZIS semiconductor, the photogenerated electrons in the valance band (VB) are excited to the conduction band (CB), resulting in the photogenerated electron and hole pairs [61]. The photogenerated holes attack the water to form $\bullet\text{OH}$ radicals and H^+ ions because the position of VB is more positive than the oxidation potential ($E(\text{H}_2\text{O}/\bullet\text{OH}) = 2.37 \text{ V}$). In the second stage, absorbed CH_3COOH dissociates as CH_3COO^- species and H^+ ions on the surface of ZIS. The holes and $\bullet\text{OH}$ radicals attack the produced CH_3COO^- species to form $\bullet\text{CH}_3$ radicals, known as the photo-Kolbe reaction [25,62]. The active $\bullet\text{CH}_3$ radicals then react with H_2O or H^+ to produce CH_4 molecules [63].

The assistance of CTAB enhanced the photocatalytic efficiency of ZnIn_2S_4 by improving its morphology and migration capability and boosted the dispersion and stabilization properties of ZnIn_2S_4 by forming a protective layer that produced steric hindrances to prevent aggregation. Herein, the (006) diffraction peak moved to a lower angle in the presence of CTAB, which indicated the enlargement of interlayer distance along the c-axis [21,22].

The photogenerated charge transfer resistance was significantly lower in ZIS-3.75 compared to that with ZIS-0 [16,64].

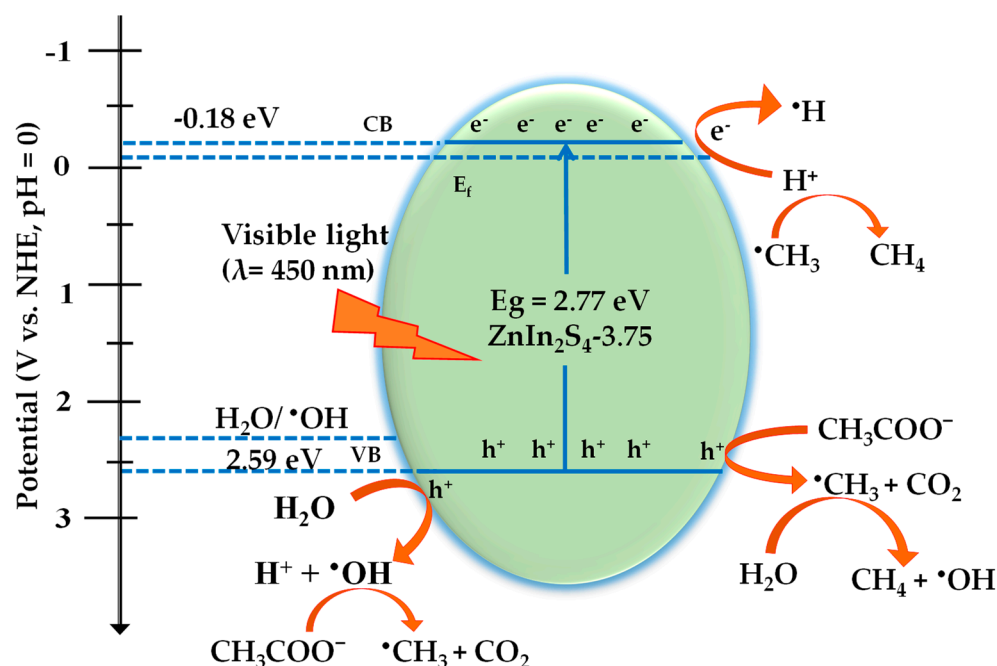
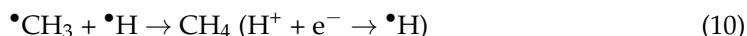
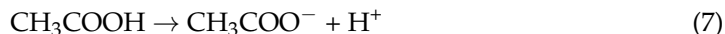


Figure 11. Proposed mechanism of photocatalytic methane production from a CH_3COOH solution with ZIS-3.75.

Mozia et al. reported improved methane production from acetic acid by direct and suspended TiO_2 under the N_2 atmosphere and UV light irradiation (Table 2) [65,66]. Further, they utilized Fe-modified TiO_2 for methane production under the same conditions [24]. Asal et al. studied the methane production from acetic acid over La^{3+} -modified TiO_2 [67]. The modification of TiO_2 with Cu significantly enhanced photocatalytic methane production from the acetic acid solution under UV light irradiation, as reported by Heciak et al. [25]. In the present work, we have succeeded in photocatalytic CH_4 production with CTAB-assisted ZnIn_2S_4 from the acetic acid solution under atmospheric conditions under visible light irradiation (450 nm).

Table 2. Comparison of photocatalytic methane production from acetic acid.

Photocatalyst (mg/mL)	CH_3COOH conc. (M)	Light Source (nm)	CH_4 ($\mu\text{mol h}^{-1} \text{g}^{-1}$)	Ref.
TiO_2 (1.0)	1.0	Hg lamp (365)	108	[65]
TiO_2 (1.86)	1.0	Hg lamp (365)	72	[66]
Fe- TiO_2 (1.0)	1.0	Hg lamp (365)	91	[24]
Sm^{3+} - TiO_2 (1.0)	1.0	UV lamp (365)	124	[67]
Cu- TiO_2 (1.0)	1.0	Hg lamp (365)	590	[25]
CTAB assisted ZnIn_2S_4 (1.87)	1.0	LED (450)	0.11	This work

6. Conclusions

In this study, a set of pure and CTAB-assisted ZIS has been hydrothermally synthesized for photocatalytic CH₄ production. The structural, optical, and electrochemical properties were characterized by XRD, FTIR, SEM, DRS, EIS, and TPCR analyses. All the photocatalysts were applied to convert the aqueous solution of acetic acid into methane under visible light irradiation without using any noble metal. One mol L^{−1} aqueous solution of acetic acid with pH = 3.0 at 50 °C was a favorable condition for the highest amount of methane production. The migration efficiency was improved with the assistance of CTAB. The electrochemical analysis confirmed the decreased charge transfer resistance and increased photocurrent response properties due to the use of surfactant. The photocatalytic CH₄ production from acetic acid was 1.76 times better for the ZIS-3.75 photocatalyst than that obtained with pure ZIS. The methane production steps have been depicted using a possible reaction mechanism.

Author Contributions: M.U.; conceptualization, methodology, data curation, formal analysis, investigation, and writing—original draft, review, and editing. M.F.A.; formal analysis and investigation. M.F.; formal analysis and review and editing. I.T.; formal analysis and review and editing. H.K.; writing—review and editing. S.K.; conceptualization, writing—review and editing, and supervision. All authors have read and agreed to the published version of the manuscript.

Funding: This research was partially funded by a Grant-in-Aid for Scientific Research (B) 21H03642 from the Ministry of Education, Culture, Sports, Science and Technology of Japan.

Data Availability Statement: The data presented in this study are available on request from the corresponding author.

Acknowledgments: The authors acknowledge Yukiko Fujita for their support with SEM and TEM analysis.

Conflicts of Interest: All authors have declared that (i) no support, financial or otherwise, has been received from any organization that may have an interest in the submitted work and (ii) there are no other relationships or activities that could appear to have influenced the submitted work. All experiments were conducted at Mie University. Any opinions, findings, conclusions, or recommendations expressed in this paper are those of the authors and do not necessarily reflect the view of the supporting organizations.

References

- Chen, X.; Shen, S.; Guo, L.; Mao, S.S. Semiconductor-Based Photocatalytic Hydrogen Generation. *Chem. Rev.* **2010**, *110*, 6503–6570. [\[CrossRef\]](#)
- Chauhan, D.K.; Sharma, N.; Kailasam, K. A Critical Review on Emerging Photocatalysts for Syngas Generation via CO₂ Reduction under Aqueous Media: A Sustainable Paradigm. *Mater. Adv.* **2022**, *3*, 5274–5298. [\[CrossRef\]](#)
- Chandra, R.; Takeuchi, H.; Hasegawa, T. Methane Production from Lignocellulosic Agricultural Crop Wastes: A Review in Context to Second Generation of Biofuel Production. *Renew. Sustain. Energy Rev.* **2012**, *16*, 1462–1476. [\[CrossRef\]](#)
- Roy, S.C.; Varghese, O.K.; Paulose, M.; Grimes, C.A. Toward Solar Fuels: Photocatalytic Conversion of Carbon Dioxide to Hydrocarbons. *ACS Nano* **2010**, *4*, 1259–1278. [\[CrossRef\]](#)
- Yang, R.; Mei, L.; Fan, Y.; Zhang, Q.; Zhu, R.; Amal, R.; Yin, Z.; Zeng, Z. ZnIn₂S₄-Based Photocatalysts for Energy and Environmental Applications. *Small Methods* **2021**, *5*, 2100887. [\[CrossRef\]](#)
- Amin, A.M.; Croiset, E.; Epling, W. Review of Methane Catalytic Cracking for Hydrogen Production. *Int. J. Hydrogen Energy* **2011**, *36*, 2904–2935. [\[CrossRef\]](#)
- Yang, Y.-Y.; Feng, H.-P.; Zhang, X.-G.; Guo, H.; Wen, X.-J.; Sui, L.; Dong, Z.-T.; Yan, M.; Niu, C.-G. Regulating and Protecting of Oxygen Vacancy Endow MoO₃-X@Zn₂In₂S₅ S-Scheme Core-Shell Heterojunction with High-Efficiency Organic Pollutant Removal and Bacterial Disinfection: Correlation of Pollutant Active Sites to Degradation Pathways. *Chem. Eng. J.* **2024**, *490*, 151309. [\[CrossRef\]](#)
- Wang, J.; Sun, S.; Zhou, R.; Li, Y.; He, Z.; Ding, H.; Chen, D.; Ao, W. A Review: Synthesis, Modification and Photocatalytic Applications of ZnIn₂S₄. *J. Mater. Sci. Technol.* **2021**, *78*, 1–19. [\[CrossRef\]](#)
- Lei, Z.; Ma, G.; Liu, M.; You, W.; Yan, H.; Wu, G.; Takata, T.; Hara, M.; Domen, K.; Li, C. Sulfur-Substituted and Zinc-Doped In(OH)₃: A New Class of Catalyst for Photocatalytic H₂ Production from Water under Visible Light Illumination. *J. Catal.* **2006**, *237*, 322–329. [\[CrossRef\]](#)

10. Yadav, G.; Ahmaruzzaman, M. ZnIn_2S_4 and ZnIn_2S_4 Based Advanced Hybrid Materials: Structure, Morphology and Applications in Environment and Energy. *Inorg. Chem. Commun.* **2022**, *138*, 109288. [\[CrossRef\]](#)
11. Du, C.; Zhang, Q.; Lin, Z.; Yan, B.; Xia, C.; Yang, G. Half-Unit-Cell ZnIn_2S_4 Monolayer with Sulfur Vacancies for Photocatalytic Hydrogen Evolution. *Appl. Catal. B* **2019**, *248*, 193–201. [\[CrossRef\]](#)
12. Zhang, G.; Wu, H.; Chen, D.; Li, N.; Xu, Q.; Li, H.; He, J.; Lu, J. A Mini-Review on ZnIn_2S_4 -Based Photocatalysts for Energy and Environmental Application. *Green Energy Environ.* **2022**, *7*, 176–204. [\[CrossRef\]](#)
13. Khan, M.M.; Adil, S.F.; Al-Mayouf, A. Metal Oxides as Photocatalysts. *J. Saudi Chem. Soc.* **2015**, *19*, 462–464. [\[CrossRef\]](#)
14. Gao, M.-R.; Xu, Y.-F.; Jiang, J.; Yu, S.-H. Nanostructured Metal Chalcogenides: Synthesis, Modification and Applications in Energy Conversion and Storage Devices. *Chem. Soc. Rev.* **2013**, *42*, 2986. [\[CrossRef\]](#)
15. Fu, J.; Yu, J.; Jiang, C.; Cheng, B. g- C_3N_4 -Based Heterostructured Photocatalysts. *Adv. Energy Mater.* **2018**, *8*, 1701503. [\[CrossRef\]](#)
16. Yan, Y.; Chen, Z.; Cheng, X.; Shi, W. Research Progress of ZnIn_2S_4 -Based Catalysts for Photocatalytic Overall Water Splitting. *Catalysts* **2023**, *13*, 967. [\[CrossRef\]](#)
17. Shen, S.; Guo, P.; Zhao, L.; Du, Y.; Guo, L. Insights into Photoluminescence Property and Photocatalytic Activity of Cubic and Rhombohedral ZnIn_2S_4 . *J. Solid State Chem.* **2011**, *184*, 2250–2256. [\[CrossRef\]](#)
18. Gao, C.; Xie, Y.; Chen, Y.; Ling, Y.; Ma, Y.; Zhang, Y.; Shao, Y. Construction of $\text{ZnIn}_2\text{S}_4/\text{Bi}_2\text{MoO}_6$ Heterojunction Enhancement Photocatalytic Hydrogen Evolution Performance under Visible Light. *Int. J. Hydrogen Energy* **2024**, *52*, 90–99. [\[CrossRef\]](#)
19. Zheng, X.; Song, Y.; Liu, Y.; Yang, Y.; Wu, D.; Yang, Y.; Feng, S.; Li, J.; Liu, W.; Shen, Y.; et al. ZnIn_2S_4 -Based Photocatalysts for Photocatalytic Hydrogen Evolution via Water Splitting. *Coord. Chem. Rev.* **2023**, *475*, 214898. [\[CrossRef\]](#)
20. Zhong, X.; Zhu, Y.; Jiang, M.; Sun, Q.; Yao, J. Dual Defective K-Doping and Cyano Group Sites on Carbon Nitride Nanotubes for Improved Hydrogen Photo-Production. *Energy Fuels* **2023**, *37*, 5448–5456. [\[CrossRef\]](#)
21. Shen, S.; Zhao, L.; Guo, L. Cetyltrimethylammoniumbromide (CTAB)-Assisted Hydrothermal Synthesis of ZnIn_2S_4 as an Efficient Visible-Light-Driven Photocatalyst for Hydrogen Production. *Int. J. Hydrogen Energy* **2008**, *33*, 4501–4510. [\[CrossRef\]](#)
22. Shen, S.; Zhao, L.; Guo, L. Crystallite, Optical and Photocatalytic Properties of Visible-Light-Driven ZnIn_2S_4 Photocatalysts Synthesized via a Surfactant-Assisted Hydrothermal Method. *Mater. Res. Bull.* **2009**, *44*, 100–105. [\[CrossRef\]](#)
23. Kraeutler, B.; Bard, A.J. Photoelectrosynthesis of Ethane from Acetate Ion at an N-Type Titanium Dioxide Electrode. The Photo-Kolbe Reaction. *J. Am. Chem. Soc.* **1977**, *99*, 7729–7731. [\[CrossRef\]](#)
24. Mozia, S.; Heciak, A.; Morawski, A.W. Photocatalytic Acetic Acid Decomposition Leading to the Production of Hydrocarbons and Hydrogen on Fe-Modified TiO_2 . *Catal. Today* **2011**, *161*, 189–195. [\[CrossRef\]](#)
25. Heciak, A.; Morawski, A.W.; Grzmil, B.; Mozia, S. Cu-Modified TiO_2 Photocatalysts for Decomposition of Acetic Acid with Simultaneous Formation of C1–C3 Hydrocarbons and Hydrogen. *Appl. Catal. B* **2013**, *140*, 108–114. [\[CrossRef\]](#)
26. Amorós-Pérez, A.; Cano-Casanova, L.; Lillo-Ródenas, M.Á.; Román-Martínez, M.C. Cu/ TiO_2 Photocatalysts for the Conversion of Acetic Acid into Biogas and Hydrogen. *Catal. Today* **2017**, *287*, 78–84. [\[CrossRef\]](#)
27. Gou, X.; Cheng, F.; Shi, Y.; Zhang, L.; Peng, S.; Chen, J.; Shen, P. Shape-Controlled Synthesis of Ternary Chalcogenide ZnIn_2S_4 and $\text{CuIn}(\text{S},\text{Se})_2$ Nano-/Microstructures via Facile Solution Route. *J. Am. Chem. Soc.* **2006**, *128*, 7222–7229. [\[CrossRef\]](#) [\[PubMed\]](#)
28. Chen, Z.; Guo, F.; Sun, H.; Shi, Y.; Shi, W. Well-Designed Three-Dimensional Hierarchical Hollow Tubular g- $\text{C}_3\text{N}_4/\text{ZnIn}_2\text{S}_4$ Nanosheets Heterostructure for Achieving Efficient Visible-Light Photocatalytic Hydrogen Evolution. *J. Colloid Interface Sci.* **2022**, *607*, 1391–1401. [\[CrossRef\]](#) [\[PubMed\]](#)
29. Zhang, Z.; Liu, K.; Feng, Z.; Bao, Y.; Dong, B. Hierarchical Sheet-on-Sheet $\text{ZnIn}_2\text{S}_4/\text{g-C}_3\text{N}_4$ Heterostructure with Highly Efficient Photocatalytic H_2 Production Based on Photoinduced Interfacial Charge Transfer. *Sci. Rep.* **2016**, *6*, 19221. [\[CrossRef\]](#)
30. Shettigar, R.R.; Misra, N.M.; Patel, K. Cationic Surfactant (CTAB) a Multipurpose Additive in Polymer-Based Drilling Fluids. *J. Pet. Explor. Prod. Technol.* **2018**, *8*, 597–606. [\[CrossRef\]](#)
31. Elfeky, S.A.; Mahmoud, S.E.; Youssef, A.F. Applications of CTAB Modified Magnetic Nanoparticles for Removal of Chromium (VI) from Contaminated Water. *J. Adv. Res.* **2017**, *8*, 435–443. [\[CrossRef\]](#)
32. Ramos Guivar, J.A.; Sanches, E.A.; Magon, C.J.; Ramos Fernandes, E.G. Preparation and Characterization of Cetyltrimethylammonium Bromide (CTAB)-Stabilized Fe_3O_4 Nanoparticles for Electrochemistry Detection of Citric Acid. *J. Electroanal. Chem.* **2015**, *755*, 158–166. [\[CrossRef\]](#)
33. Viana, R.B.; da Silva, A.B.F.; Pimentel, A.S. Infrared Spectroscopy of Anionic, Cationic, and Zwitterionic Surfactants. *Adv. Phys. Chem.* **2012**, *2012*, 903272. [\[CrossRef\]](#)
34. Predoi, S.-A.; Ciobanu, C.S.; Motelica-Heino, M.; Chifiriuc, M.C.; Badea, M.L.; Iconaru, S.L. Preparation of Porous Hydroxyapatite Using Cetyl Trimethyl Ammonium Bromide as Surfactant for the Removal of Lead Ions from Aquatic Solutions. *Polymers* **2021**, *13*, 1617. [\[CrossRef\]](#)
35. Lin, C.; Fan, B.; Zhang, J.X.; Yang, X.; Zhang, H. Study on Lead Ion Wastewater Treatment of Self-Assembled Film. *Desalination Water Treat.* **2016**, *57*, 21627–21633. [\[CrossRef\]](#)
36. Shao, Y.; Hu, J.; Yang, T.; Yang, X.; Qu, J.; Xu, Q.; Li, C.M. Significantly Enhanced Photocatalytic In-Situ H_2O_2 Production and Consumption Activities for Efficient Sterilization by $\text{ZnIn}_2\text{S}_4/\text{g-C}_3\text{N}_4$ Heterojunction. *Carbon* **2022**, *190*, 337–347. [\[CrossRef\]](#)
37. Kumar, Y.; Sudhaik, A.; Sharma, K.; Sonu; Raizada, P.; Aslam Parwaz Khan, A.; Nguyen, V.-H.; Ahamad, T.; Singh, P.; Asiri, A.M. Construction of Magnetically Separable Novel Arrow down Dual S-Scheme $\text{ZnIn}_2\text{S}_4/\text{BiOCl}/\text{FeVO}_4$ Heterojunction for Improved Photocatalytic Activity. *J. Photochem. Photobiol. A Chem.* **2023**, *435*, 114326. [\[CrossRef\]](#)

38. Zhong, Y.; Shi, J.; Li, K.; Guo, H.; Yan, L.; Luo, S. Fabrication and Immobilization of Heteropoly Acids (HPAs) and Hexadecyl Trimethyl Ammonium Bromide (CTAB) Co-Modified Ternary Zinc Indium Sulfide (ZnIn_2S_4): Capture Photogenerated Electrons and Pollutant Molecules by Co-Photocatalyst for Enhancing the Photocatalytic Ability. *Appl. Surf. Sci.* **2023**, *624*, 157105. [\[CrossRef\]](#)
39. Yuan, L.; Li, Y.-H.; Tang, Z.-R.; Gong, J.; Xu, Y.-J. Defect-Promoted Visible Light-Driven C–C Coupling Reactions Pairing with CO_2 Reduction. *J. Catal.* **2020**, *390*, 244–250. [\[CrossRef\]](#)
40. AlOthman, Z. A Review: Fundamental Aspects of Silicate Mesoporous Materials. *Materials* **2012**, *5*, 2874–2902. [\[CrossRef\]](#)
41. Li, L.; Ma, D.; Xu, Q.; Huang, S. Constructing Hierarchical $\text{ZnIn}_2\text{S}_4/\text{g-C}_3\text{N}_4$ S-Scheme Heterojunction for Boosted CO_2 Photoreduction Performance. *J. Chem. Eng.* **2022**, *437*, 135153. [\[CrossRef\]](#)
42. Zhang, X.; Yang, P.; Chen, H.S.; Jiang, S.P. Carbon Layer Derived Carrier Transport in $\text{Co/g-C}_3\text{N}_4$ Nanosheet Junctions for Efficient H_2O_2 Production and NO Removal. *J. Chem. Eng.* **2024**, *479*, 147609. [\[CrossRef\]](#)
43. Tsuji, I.; Kato, H.; Kudo, A. Photocatalytic Hydrogen Evolution on $\text{ZnS-CuInS}_2\text{-AgInS}_2$ Solid Solution Photocatalysts with Wide Visible Light Absorption Bands. *Chem. Mater.* **2006**, *18*, 1969–1975. [\[CrossRef\]](#)
44. Huang, W.; Li, Z.; Wu, C.; Zhang, H.; Sun, J.; Li, Q. Delaminating Ti_3C_2 MXene by Blossom of ZnIn_2S_4 Microflowers for Noble-Metal-Free Photocatalytic Hydrogen Production. *J. Mater. Sci. Technol.* **2022**, *120*, 89–98. [\[CrossRef\]](#)
45. Yang, Y.; Niu, W.; Dang, L.; Mao, Y.; Wu, J.; Xu, K. Recent Progress in Doped $\text{g-C}_3\text{N}_4$ Photocatalyst for Solar Water Splitting: A Review. *Front. Chem.* **2022**, *10*, 955065. [\[CrossRef\]](#) [\[PubMed\]](#)
46. Uzzaman, M.; Suhag, M.H.; Katsumata, H.; Tateishi, I.; Furukawa, M.; Kaneco, S. A Graphitic Carbon Nitride Photocatalyst with a Benzene-Ring-Modified Isotype Heterojunction for Visible-Light-Driven Hydrogen Production. *Catal. Sci. Technol.* **2024**, *14*, 267–278. [\[CrossRef\]](#)
47. Chang, B.-Y.; Park, S.-M. Electrochemical Impedance Spectroscopy. *Annu. Rev. Anal. Chem.* **2010**, *3*, 207–229. [\[CrossRef\]](#)
48. Zhang, D.; Lv, S.; Luo, Z. A Study on the Photocatalytic Degradation Performance of a $[\text{KNbO}_3]_{0.9}\text{-}[\text{BaNi}_{0.5}\text{Nb}_{0.5}\text{O}_{3-\delta}]_{0.1}$ Perovskite. *RSC Adv.* **2020**, *10*, 1275–1280. [\[CrossRef\]](#) [\[PubMed\]](#)
49. Yamamoto, A.; Mizuno, Y.; Teramura, K.; Shishido, T.; Tanaka, T. Effects of Reaction Temperature on the Photocatalytic Activity of Photo-SCR of NO with NH_3 over a TiO_2 Photocatalyst. *Catal. Sci. Technol.* **2013**, *3*, 1771. [\[CrossRef\]](#)
50. Chen, Y.-W.; Hsu, Y.-H. Effects of Reaction Temperature on the Photocatalytic Activity of TiO_2 with Pd and Cu Cocatalysts. *Catalysts* **2021**, *11*, 966. [\[CrossRef\]](#)
51. Azad, K.; Gajanan, P. Photodegradation of Methyl Orange in Aqueous Solution by the Visible Light Active Co:La:TiO_2 Nanocomposite. *Chem. Sci. J.* **2017**, *8*, 1000164–1000174. [\[CrossRef\]](#)
52. Zhang, J.; Yuan, G.; Wang, H.; Wu, J.; Yang, G.; Jia, Q.; Zhang, S.; Li, F.; Zhang, H. Preparation of Core/Shell-Structured $\text{ZnFe}_2\text{O}_4@\text{ZnIn}_2\text{S}_4$ Catalysts and Its Ultrafast Microwave Catalytic Reduction Performance for Aqueous Cr(VI) . *J. Chem. Eng.* **2023**, *451*, 138182. [\[CrossRef\]](#)
53. Hassaan, M.A.; El-Nemr, M.A.; Elkatory, M.R.; Ragab, S.; Niculescu, V.-C.; El Nemr, A. Principles of Photocatalysts and Their Different Applications: A Review. *Top. Curr. Chem.* **2023**, *381*, 31. [\[CrossRef\]](#) [\[PubMed\]](#)
54. An, T.; Xiong, Y.; Li, G.; Zha, C.; Zhu, X. Synergetic Effect in Degradation of Formic Acid Using a New Photoelectrochemical Reactor. *J. Photochem. Photobiol. A Chem.* **2002**, *152*, 155–165. [\[CrossRef\]](#)
55. Chen, Q.; Song, J.M.; Pan, F.; Xia, F.L.; Yuan, J.Y. The Kinetics of Photocatalytic Degradation of Aliphatic Carboxylic Acids in an UV/ TiO_2 Suspension System. *Environ. Technol.* **2009**, *30*, 1103–1109. [\[CrossRef\]](#) [\[PubMed\]](#)
56. Khan, S.A.; Jain, M.; Pant, K.K.; Ziora, Z.M.; Blaskovich, M.A.T. Photocatalytic Degradation of Parabens: A Comprehensive Meta-Analysis Investigating the Environmental Remediation Potential of Emerging Pollutant. *Sci. Total Environ.* **2024**, *920*, 171020. [\[CrossRef\]](#) [\[PubMed\]](#)
57. Chen, Q.; Chang, J.; Li, L.; Yuan, J.Y. A New Kinetic Model of Photocatalytic Degradation of Formic Acid in UV/ TiO_2 Suspension System with in-Situ Monitoring. *React. Kinet. Catal. Lett.* **2008**, *93*, 157–164. [\[CrossRef\]](#)
58. Serpone, N.; Martin, J.; Horikoshi, S.; Hidaka, H. Photocatalyzed Oxidation and Mineralization of C1–C5 Linear Aliphatic Acids in UV-Irradiated Aqueous Titania Dispersions—Kinetics, Identification of Intermediates and Quantum Yields. *J. Photochem. Photobiol. A Chem.* **2005**, *169*, 235–251. [\[CrossRef\]](#)
59. Guillard, C. Photocatalytic Degradation of Butanoic Acid. *J. Photochem. Photobiol. A Chem.* **2000**, *135*, 65–75. [\[CrossRef\]](#)
60. Franch, M.I.; Ayllón, J.A.; Peral, J.; Domènech, X. Photocatalytic Degradation of Short-Chain Organic Diacids. *Catal. Today* **2002**, *76*, 221–233. [\[CrossRef\]](#)
61. Shi, J.; Yuan, T.; Zheng, M.; Wang, X. Metal-Free Heterogeneous Semiconductor for Visible-Light Photocatalytic Decarboxylation of Carboxylic Acids. *ACS Catal.* **2021**, *11*, 3040–3047. [\[CrossRef\]](#)
62. Tezuka, K.; Kogure, M.; Shan, Y.J. Photocatalytic Degradation of Acetic Acid on Spinel Ferrites MFe_2O_4 ($\text{M} = \text{Mg, Zn, and Cd}$). *Catal. Commun.* **2014**, *48*, 11–14. [\[CrossRef\]](#)
63. Zheng, X.-J.; Wei, L.-F.; Zhang, Z.-H.; Jiang, Q.-J.; Wei, Y.-J.; Xie, B.; Wei, M.-B. Research on Photocatalytic H_2 Production from Acetic Acid Solution by Pt/TiO_2 Nanoparticles under UV Irradiation. *Int. J. Hydrogen Energy* **2009**, *34*, 9033–9041. [\[CrossRef\]](#)
64. Tang, M.; Yin, W.; Zhang, F.; Liu, X.; Wang, L. The Potential Strategies of ZnIn_2S_4 -Based Photocatalysts for the Enhanced Hydrogen Evolution Reaction. *Front. Chem.* **2022**, *10*, 959414. [\[CrossRef\]](#)
65. Mozia, S.; Heciak, A.; Morawski, A.W. The Influence of Physico-Chemical Properties of TiO_2 on Photocatalytic Generation of C1–C3 Hydrocarbons and Hydrogen from Aqueous Solution of Acetic Acid. *Appl. Catal. B* **2011**, *104*, 21–29. [\[CrossRef\]](#)

66. Mozia, S.; Heciak, A.; Darowna, D.; Morawski, A.W. A Novel Suspended/Supported Photoreactor Design for Photocatalytic Decomposition of Acetic Acid with Simultaneous Production of Useful Hydrocarbons. *J. Photochem. Photobiol. A Chem.* **2012**, *236*, 48–53. [[CrossRef](#)]
67. Asal, S.; Saif, M.; Hafez, H.; Mozia, S.; Heciak, A.; Moszyński, D.; Abdel-Mottaleb, M.S.A. Photocatalytic Generation of Useful Hydrocarbons and Hydrogen from Acetic Acid in the Presence of Lanthanide Modified TiO₂. *Int. J. Hydrogen Energy* **2011**, *36*, 6529–6537. [[CrossRef](#)]

Disclaimer/Publisher's Note: The statements, opinions and data contained in all publications are solely those of the individual author(s) and contributor(s) and not of MDPI and/or the editor(s). MDPI and/or the editor(s) disclaim responsibility for any injury to people or property resulting from any ideas, methods, instructions or products referred to in the content.